nature communications

Article

https://doi.org/10.1038/s41467-025-67803-4

In vivo electrochemical reduction-induced reconfiguration of Prussian blue for metal counterion-free potassium removal in hyperkalemia

Received: 2 March 2025

Accepted: 9 December 2025

Published online: 23 December 2025

Check for updates

Yuge Wu[1,3], Liang Xiang[1,2,3], Xin Zhao[2], Tianzhi Liu[1], Yao Xiao[1], Xiaolin Cui[1], Futao Tang[1], Zhen Liu[1], Ju Zeng[1] & Shiyi Zhang[1]

Hyperkalemia, a life-threatening metabolic disorder, persists as unmet medical need since current first-line pharmacotherapy—ion-exchange potassium binders—inevitably release metal counterions (e.g., sodium) that paradoxically aggravate metabolic comorbidities. Here, we present a paradigm-shifting in vivo reduction-induced ion-selective adsorption (IRISA) strategy, utilizing Prussian Blue and Vitamin C for metal counterion-free potassium removal. IRISA leverages VC to trigger structural remodeling of PB through Fe reduction, inducing spin-state transitions and lattice reconfiguration that create K^+-specific channels with optimized charge distribution. Spectroscopic studies and DFT calculations reveal K^+ adsorption through electron density redistribution at coordinatively unsaturated Fe sites. This ion adsorption mechanism enables selective adsorption of K^+ without metal counterion release. In three male animal models of hyperkalemia, it rapidly normalizes serum K^+ while preserving Na^+ homeostasis, offering a critical advantage over current first-line therapies that perturb sodium balance. Our findings establish a new paradigm for electrolyte disorder treatment using in vivo reduction-induced material reconfiguration, merging electrochemical principles with precision medicine.

Hyperkalemia is a life-threatening metabolic disorder characterized by elevated serum K^+ levels[1]. It is particularly common in individuals with comorbidities such as impaired renal function, cancer, liver failure, severe diabetes, and polypharmacy[2–6]. Approximately 90% of K^+ is excreted via the kidneys in physiological condition[7,8]. Decreased renal function leads to potassium retention, increasing the risk of hyperkalemia[9]. Current treatments, including potassium binders like sodium polystyrene sulfonate (SPS, Kayexalate®), calcium polystyrene sulfonate (CPS, Kalimate®), sodium zirconium cyclosilicate (SZC, Lokelma™) and patiromer sorbitex calcium (patiromer, Veltassa®), promote K^+ removal via the gastrointestinal (GI) tract, compensating for reduced renal excretion[10–14]. However, SPS and CPS carry well-documented risks of severe GI complications, particularly colonic necrosis and intestinal perforation[15–18]. While patiromer is an alternative, it exhibits critical limitations relative to the inorganic crystalline matrix of SZC, including delayed therapeutic onset (7–48 h), significant drug interaction potential, nonspecific binding (e.g., Mg^{2+}), and higher GI adverse event rates, making it unsuitable for emergent management[19,20]. Notably, all current therapeutic binders rely on ion-exchange mechanism, releasing metal counterions that can disrupt the fluid balance and cause metabolic disturbances, particularly in patients with underlying conditions[21]. Even SZC releases Na^+, which increases

[1]School of Biomedical Engineering, Shanghai Jiao Tong University, Shanghai, PR China. [2]Suzhou Intelligem Pharmaceutical Technology Co. Ltd, Suzhou, PR China. [3]These authors contributed equally: Yuge Wu, Liang Xiang. e-mail: zhangshiyi@sjtu.edu.cn

the risk of edema, fluid retention and hypertension, especially in patients with chronic kidney disease or heart failure[22–24]. In previous work, we developed a nanoporous material based on K^+-NH_4^+ ion exchange, where NH_4^+ replaces Na^+. The release of NH_4^+ inhibits Na^+ reabsorption while simultaneously promoting K^+ reabsorption[25]. This mechanism exacerbates salt wasting, consequently resulting in suboptimal performance in managing conditions such as Pseudohypoaldosteronism type I (PHA-1) complicated by hyperkalemia[25,26]. Additionally, in patients with abnormal nitrogen metabolism complicated by hyperkalemia, releasing NH_4^+ increases the burden on the liver, posing additional risks[4,27]. To date, no potassium binder has been developed that completely avoids metal counterion release. Therefore, a novel potassium adsorption approach that minimizes metal counterion-related complications is urgently needed.

Prussian blue (PB), an organometallic-like framework with large interstitial sites that facilitates high K^+ mobility, has shown promise as a host material for potassium-ion batteries[28–30]. This application leverages a fundamental property shared by PB and its analogue: their well-established ability to electrochemically intercalate and deintercalate various alkali metal ions, as extensively studied in systems like sodium-ion batteries[31]. In potassium-ion batteries, PB serves as the positive electrode, where significant amounts of K^+ are inserted during the voltage-driven reduction process of electrochemical reaction[32]. The ability of PB to insert K^+ is primarily due to the variable oxidation states of iron, which help maintain charge balance and enable efficient K^+ selection and adsorption[33,34]. The insolubility of PB allows for gut-restricted use in humans, offering a unique safety profile for treating Cesium and Thallium poisoning, with zero systemic exposure[35–37]. Given these advantageous characteristics, including high K^+ diffusion coefficient, remarkable storage capacity and structural stability, PB, as an FDA-approved drug, aligns well with therapeutic approaches of potassium binders for hyperkalemia[38–40]. However, K^+ adsorption capacity of single PB is limited in both single-ion and multi-element systems, and it involves counterion release[41]. Therefore, PB cannot be directly used for hyperkalemia management.

This paradox motivates our reimagining of in vivo and electrochemical interfaces, we could use antioxidant to replicate voltage-driven ion insertion principles. Herein, by bridging electrochemical insertion concepts with gut-restricted therapeutic design, we present an innovative in vivo reduction-induced ion-selective adsorption (IRISA) strategy for hyperkalemia treatment. Our IRISA strategy combines PB with vitamin C (VC), a well-known safe antioxidant, to enhance K^+ adsorption capacity and prevent metal counterion release of PB. VC can reduce Fe, facilitating K^+ binding within diffusion channels of PB[42,43]. Material characterizations and theoretical calculations demonstrate that the presence of K^+ is essential for VC to alter the valence state of Fe in PB. The reduction of PB promotes K^+ removal from the GI tract, where it aids in maintaining K^+ transfer from blood vessels until serum K^+ levels normalize (Fig. 1a). Co-administration of PB and VC is safe and effective in both in vitro simulated solutions and three animal models. Unlike ion-exchanging binders, this strategy selectively adsorbs and removes K^+ without releasing metal

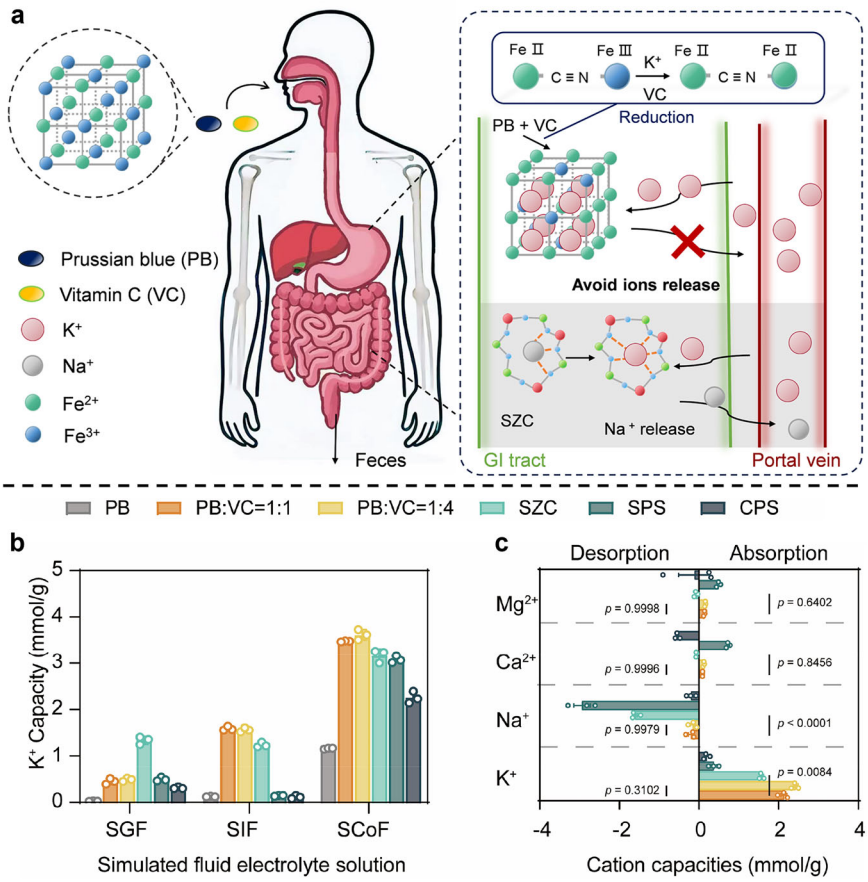

Fig. 1 | Adsorption mechanism and properties of PB + VC. a Schematic illustration of the in vivo reduction-induced ion-selective adsorption (IRISA) mechanism, depicting K^+ removal via PB + VC interaction and K^+ transfer from blood vessels in the GI tract to normalize serum K^+ levels. SZC releases Na^+ when it adsorbs K^+, as a comparison, PB + VC releases no ions. **b** K^+ capacity of PB + VC, SPS, CPS and SZC in simulated fluid electrolyte solution (independent samples, n = 3 per group). **c** Comparison of the ion-selectivity in a multi-element isoelectric (MEI) mixed solution containing K^+, Na^+, Ca^{2+}, and Mg^{2+}. The PB:VC mass ratios in PB + VC were systematically varied as 1:1 and 1:4 to evaluate composition-dependent effects (independent samples, n = 3 per group, Two-Way ANOVA using Tukey multiple comparisons test). All data are presented as the mean ± S.E.M. Significant differences are shown in the figures. Source data are provided as a Source Data file.

counterions, making it particularly beneficial for hyperkalemia patients with underlying medical conditions. In summary, our orally administered IRISA strategy, a potassium binder based on PB and VC (PB + VC), provides a promising therapeutic approach for hyperkalemia, mimicking the electrochemical reduction of an electrode. This strategy offers a novel framework with potential applications across medical therapy, electrochemistry, and beyond.

Results

The adsorption capacity of PB during reduction

The performance of potassium binders is assessed based on two critical parameters: K^+ adsorption capacity and selectivity. Prussian blue (PB), a material widely used in potassium-ion batteries, demonstrates high K^+ storage potential[19]. As an FDA-approved drug, PB is utilized for the removal of Cesium and Thallium, from the human body, with a recommended dose of 9 g day^{-1}, highlighting its gut-restricted properties and non-toxic side effects[35–37,44]. In multi-element isoelectric (MEI) mixed solutions containing K^+, Na^+, Ca^{2+}, and Mg^{2+}, PB demonstrated an excellent selectivity for K^+. However, it exhibited limited adsorption capacity (Fig. S1a). Inspired by electrochemical behavior of PB, where K^+ insertion occurs during reduction in PB as a positive electrode, we hypothesized that altering the valence state of Fe in PB might enhance its selective adsorption of K^+ by maintaining charge balance. A range of orally safe antioxidants was tested for their ability to improve K^+ adsorption. Among these, VC significantly enhanced the K^+ adsorption capacity when combined with PB in equal mass ratios (Fig. S1b). The limited efficacy of other reducing agents likely stems from their inadequate reducing power, or poor water solubility that restricts interaction with PB. Further analysis revealed that increasing VC concentration enhanced K^+ adsorption capacity of PB up to a PB:VC mass ratio of 1:1, beyond which no significant improvement was observed (Fig. S1c). Considering the renal excretion of VC, excessive doses may impose additional strain on kidney function which is already impaired. Accordingly, a PB:VC mass ratio of 1:1 was selected as an optimal and relatively safe proportion, balancing maximal adsorption capacity.

To comprehensively evaluate the K^+ adsorption efficacy of the PB and VC combination (PB + VC), we compared it with different potassium binders, in simulated GI fluids that mimic in vivo environments, including Simulated gastric fluid electrolyte solution (SGF), Simulated intestinal fluid electrolyte solution (SIF) and Simulated Colonic Fluids electrolyte solution (SCoF) (Fig. 1b). PB + VC demonstrated superior K^+ adsorption capacity compared to PB alone, SPS, CPS and comparable capacity with SZC, with no significant difference between PB:VC mass ratios of 1:1 and 1:4. Additional adsorption tests in bio-relevant simulated GI solutions demonstrated that PB + VC retained exceptional K^+ adsorption capacity and exhibited robust resistance to interference from complex components, underscoring its stability (Fig. S1d).

Given the competitive cations present in the human GI tract, we assessed the selectivity of PB + VC in the presence of interfering ions, such as Na^+, Ca^{2+}, and Mg^{2+}. exhibited minimal adsorption of ions other than K^+, demonstrating superior selectivity compared to other binder, while additionally avoiding the release of metal counterions (Fig. 1c). PB + VC demonstrates not only excellent potassium adsorption capacity but also exhibits remarkable potassium selectivity in vitro, showing negligible adsorption of Ca^{2+} and Mg^{2+} (with no significant difference compared to SZC). Importantly, unlike SZC, SPS (which releases Na^+) or CPS (which releases Ca^{2+}), PB + VC does not liberate any metal ions.

Additionally, to address potential safety concerns, we measured Fe release (Fig. S1e). Results indicated PB + VC released significantly less Fe than FDA-approved PB, confirming that VC-induced reduction does not compromise its initial structural integrity or safety profile.

Structural properties of PB before and after VC reduction

To investigate the structural changes in PB contributing to its enhanced K^+ adsorption performance upon VC addition, multiple characterizations were conducted. The XRD patterns (Fig. 2a) were consistent with Prussian blue (PDF#01-0239), indicating that the PB backbone remained stable after VC treatment during K^+ adsorption. Analysis of ion contents in the solution before and after adsorption revealed significant K^+ incorporation, accompanied by reduced lattice parameters. This reduction suggests that K^+ was incorporated into the crystal structure of PB. Significantly, analysis of the recovered liquid samples following MEI adsorption by PB + VC revealed no detectable Fe release. These observations provide evidence that, in addition to potassium adsorption, the cyanide-bridged coordination network framework of PB + VC should maintain its original chemical composition, thereby largely excluding the possibility of dissolution-recrystallization occurring during the adsorption process. Fourier transform infrared (FTIR) and Raman spectroscopy (Fig. 2b, c) revealed no peaks corresponding to organic groups such as $-CH_2-$ or $-CH_3$, confirming that VC and its reaction products did not enter the PB structure after ion adsorption. Observed peak shifts were attributed to changes in the valence state of Fe and the coordination environment of the ν(C ≡ N) bond, providing evidence of a reduction process in PB[45,46]. Room temperature ^{57}Fe Mössbauer spectra (Fig. 2d, e and Table S1) clearly revealed the presence of high-spin Fe^{2+} in VC-treated PB. By comparing the spectral area ratios of Fe species in PB and PB + VC, it can be concluded that a significant amount of mol of Fe^{3+} in each mol of PB was reduced to Fe^{2+}, resulting in a lower overall oxidation state of Fe in the PB structure.

Further analyses using X-ray photoelectron spectroscopy (XPS) and X-ray fluorescence spectroscopy (XRF) (Fig. 2f and Table S2) confirmed the successful incorporation of K^+ into VC-treated PB without release of other ions. To determine the elemental content, quantitative analysis of the solids prior to and following adsorption was carried out via inductively coupled plasma optical emission spectroscopy (ICP-OES) (Table S3). The elemental composition analysis of PB + VC, with variations ranging from 0.11 wt% to 12.1 wt% of K, revealed that the molar ratio of K to Fe in the treated sample was approximately 1:1.8. This result aligns well with the observations from Mössbauer spectroscopy, which demonstrated the reduction of Fe^{3+} and achievement of maximum theoretical K+ adsorption capacity. Based on these consistent findings, we can reasonably infer that the maximum reduction of PB by VC during the preparation process results in the chemical formula of the treated product being $K_4Fe_7C_{18}N_{18}$ (Fig. 2g). Specific surface area measurements showed that both untreated and VC-treated PB retained permanent porosity (Fig. S2), although partial filling of pores with K^+ in VC-treated PB reduced the available surface area. Both scanning electron microscopy (SEM) and transmission electron microscopy (TEM) images (Figs. 2h–j, and S3a-c, f-h) reveal uniformly-sized, well-dispersed nanocubes. Both PB and PB + VC exhibit particle sizes ranging from 30 to 70 nm, which facilitates rapid K^+ diffusion through the structure. The highly consistent particle size distribution between PB and PB + VC further confirms that K^+ adsorption was achieved not via dissolution-recrystallization, but rather through a reductive adsorption mechanism. High-angle dark-field scanning TEM (HAADF-STEM) and EDS elemental mapping (Figs. 2k, l and S3d, e, i, j) further confirmed uniform K^+ incorporation within the PB structure, reinforcing the selective K^+ adsorption capability.

Pseudo-in-situ XRD and Raman data (Fig. 3a, b) highlighted the role of VC concentration in enhancing the reduction capacity of PB. Increased VC concentration led to further decreases in PB lattice parameters and leftward shifts in the C ≡ N stretching vibration peak[47]. These results suggest that the volume of K^+ incorporated into the PB crystal lattice and the cation valence state of Fe are positively correlated with the overall reduction capacity. Cyclic voltammetry (CV) measurements (Fig. 3c) provided additional insights into the redox behavior of PB. Significant redox peaks with higher current densities and enclosed areas were observed in MEI and KCl solutions, indicating

https://doi.org/10.1038/s41467-025-67803-4

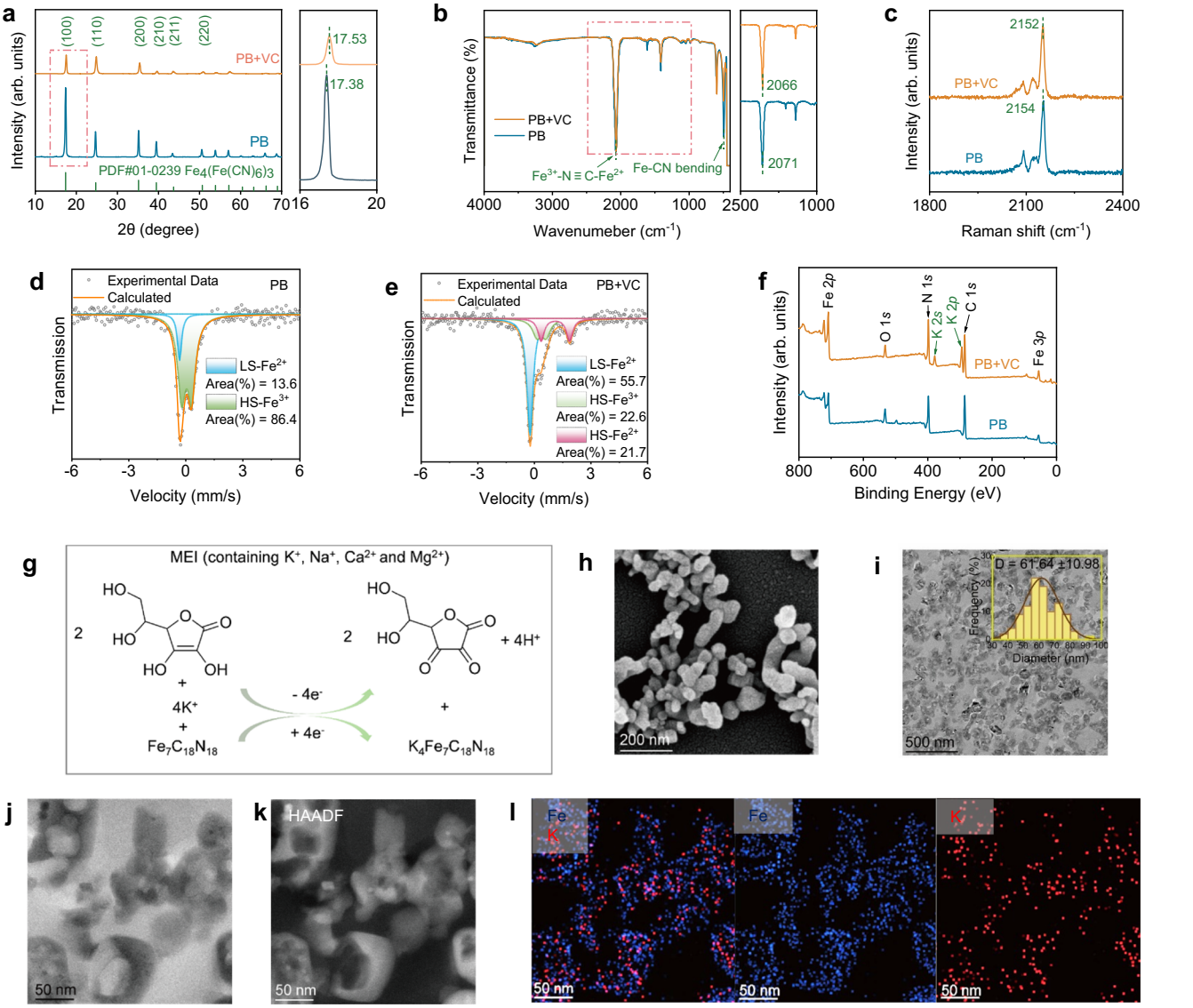

Fig. 2 | Structural and morphological characterization of PB and PB + VC after MEI treated. a XRD patterns of PB and PB + VC, right side is the enlarged (100) diffraction peak. **b** FTIR spectra of PB and PB + VC, right side is the value of wavelength (C ≡ N). **c** Raman spectrum of PB and PB + VC. **d**, **e** Mössbauer spectra of PB and PB + VC. **f** XPS wide spectrum for PB and PB + VC. **g** Schematic diagram of the reaction mechanism of adsorption/reduction mechanism. **h** SEM image showing the morphological structure of PB + VC. **i** TEM image delineating the article size distribution of PB + VC at low magnification. **j** TEM image delineating the structural details of PB + VC at high magnification. **k**, **l** HAADF-STEM image and corresponding energy dispersive spectrometer (EDS) element. All the microscopic images were repeated three times with similar results. The PB + VC sample was prepared by mixing PB and VC (1:1 mass ratio) in MEI at 37 °C with shaking (180 rpm, 2 h), followed by centrifugation, water washing, lyophilization (48 h), and finally structural characterization. In the processed PB + VC, the VC component and its oxidation products dissolve in aqueous solution, yielding a final product consisting primarily of K^+-adsorbed PB. Source data are provided as a Source Data file.

efficient ion insertion and release. The incomplete alignment of oxidation and reduction peaks reflected limited reversibility, which may promote efficient ion adsorption while hindering ion desorption, thereby enabling more thorough K^+ removal. Finally, XRD, Raman, and UV-vis characterizations of PB + VC treated with different electrolyte solutions (Fig. 3d, e, f) showed that only KCl and MEI solutions exhibited the same trend, further validating the reduction-induced adsorption mechanism.

Theoretical studies of PB selective adsorption

Density functional theory (DFT) calculations were conducted to understand the adsorption mechanism of PB for ions during the reduction process. A comparison of adsorption energies for different ions revealed that PB preferentially adsorbs K^+ over Na^+, Ca^{2+}, and Mg^{2+} (Fig. 3g). Simulating the reduced state of PB by adding four electrons significantly enhanced ion adsorption, highlighting the role of reduction in improving K^+ selectivity. The reduction mechanism was further validated by analyzing the electronic structures of cation-inserted PB. In K-PB, unoccupied spin-up states of Fe shifted below the Fermi level, suggesting that Fe more readily accept electrons and undergo redox reactions (Fig. S4).

To explore atomic-scale changes in PB during ion insertion, charge density differences were calculated to visualize the electronic state distribution (Fig. S5). In K-PB, increased charge density around Fe formed electron channels that facilitated efficient charge transfer, confirming that Fe gained electrons upon K^+ insertion. Correspondingly, Bader charge analysis (Fig. 3h, i) showed an increase in the charge on Fe, establishing Fe acts as an active redox center during the charge transfer process triggered by K^+ insertion. These charge transfer behaviors were consistent with the projected density of states

https://doi.org/10.1038/s41467-025-67803-4

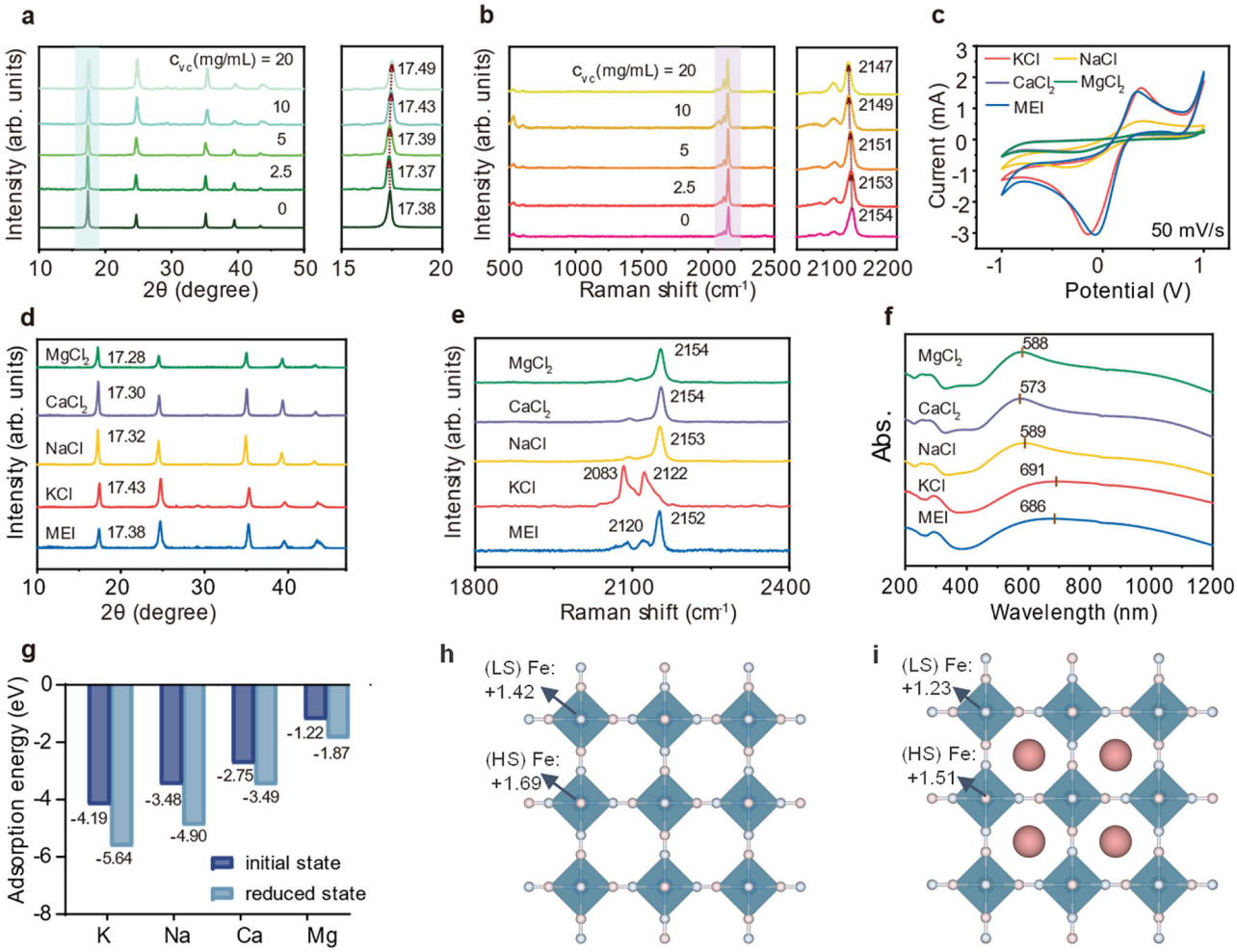

Fig. 3 | Adsorption mechanism during ion insertion. a Ex-situ XRD patterns of PB at different VC concentration, right side is the enlarged (100) diffraction peak. **b** Ex-situ Raman spectrum of PB at different VC concentration, right side is the value of wavelength (C ≡ N). **c** CV curves of PB at a scan rate of 50 mV s^{-1} in different electrolyte solutions. **d** XRD patterns of PB + VC in different electrolyte solutions. **e** Raman spectrum of PB + VC in different electrolyte solutions. **f** UV-vis spectra of PB + VC in different electrolyte solutions. **g** Adsorption energy (eV) of different ions at primary and reduced states in PB crystal. Bander charges of high-spin (HS) Fe and low-spin (LS) Fe in PB (**h**) and K-PB (**i**), Source data are provided as a Source Data file.

(PDOS) and charge density differences. Collectively, the DFT calculations provided a detailed explanation of reduction mechanism and its enhanced K^+ adsorption capacity during ion adsorption from electrolyte solutions.

Safety and therapeutic effects of PB + VC in animal models

To evaluate the feasibility of PB + VC as a potential treatment for hyperkalemia, in vitro and in vivo biosafety assays were conducted. Considering the gut-restriction of PB + VC, we tested three GI cells to assess the cytotoxicity of PB + VC, including GES-1, IEC-6 and Caco-2, based on the locations where the drug would interact[48–50]. The results of the cytotoxicity assay and calcein/PI assays revealed that PB + VC at 320 μg ml^{-1} (160 μg ml^{-1} PB + 160 μg ml^{-1} VC) is non-toxic to GI cells (Figs. 4a and S6).

In vivo biocompatibility was further assessed in healthy rats (Fig. 4b). K^+ excretion was monitored by collecting feces and urine on days 1, 8, and 15 (Fig. 4c, d). 14 days' continuous PB + VC treatment resulted in a significant reduction in urinary K^+ and an increase in fecal K^+, demonstrating that PB + VC effectively adsorbs K^+ and excretes it mostly via the feces. K^+ was primarily excreted via urine in physiological condition, PB + VC reduces the renal excretion of K^+ and potentially alleviates the burden on the kidneys[8]. Blood K^+, Na^+, Ca^{2+}, and Mg^{2+} levels, alongside urinary Na^+, Ca^{2+}, and Mg^{2+} excretion and fecal Na^+, Ca^{2+}, and Mg^{2+} content, remained within physiologically normal ranges across all experimental groups (Figs. 4d and S7). Blood gas parameters (pH, HCO_3^-, CO_2) and hematological parameters exhibited no clinically significant deviations (Figs. S8-10). Notably, Blood Fe^{2+}, transferrin, and ferritin levels also fell within normal physiological ranges (Fig. 4f–h). These findings collectively demonstrate that our therapeutic strategy, even at higher PB + VC doses, induces neither hypokalemia nor other electrolyte disturbances, acid-base imbalances, or hematological abnormalities, thereby confirming its safety profile.

Since our strategy achieves K^+ adsorption in the GI, we comprehensively assessed GI safety. The results indicated that both GI permeability and intestinal length remained within normal range (Figs. 4i and S11). Given that hyperkalemia is often accompanied with impaired renal function, we selected a therapeutic dose of 4 g kg^{-1} PB + VC (PV1: 2 g kg^{-1} PB + 2 g kg^{-1} g kg^{-1} VC) and a high dose of 12 g kg^{-1} PB + VC (PV2: 6 g kg^{-1} PB + 6 g kg^{-1} g kg^{-1} VC) to evaluate potential nephrotoxicity at different VC dosages. Urinalysis and blood biochemical parameters showed no significant differences compared to the control group, demonstrating that even at three times the therapeutic dose, VC did not cause additional renal burden or toxicity (Figs. 4j–m and S12-14). Histopathological analysis through hematoxylin and eosin (H&E)

https://doi.org/10.1038/s41467-025-67803-4

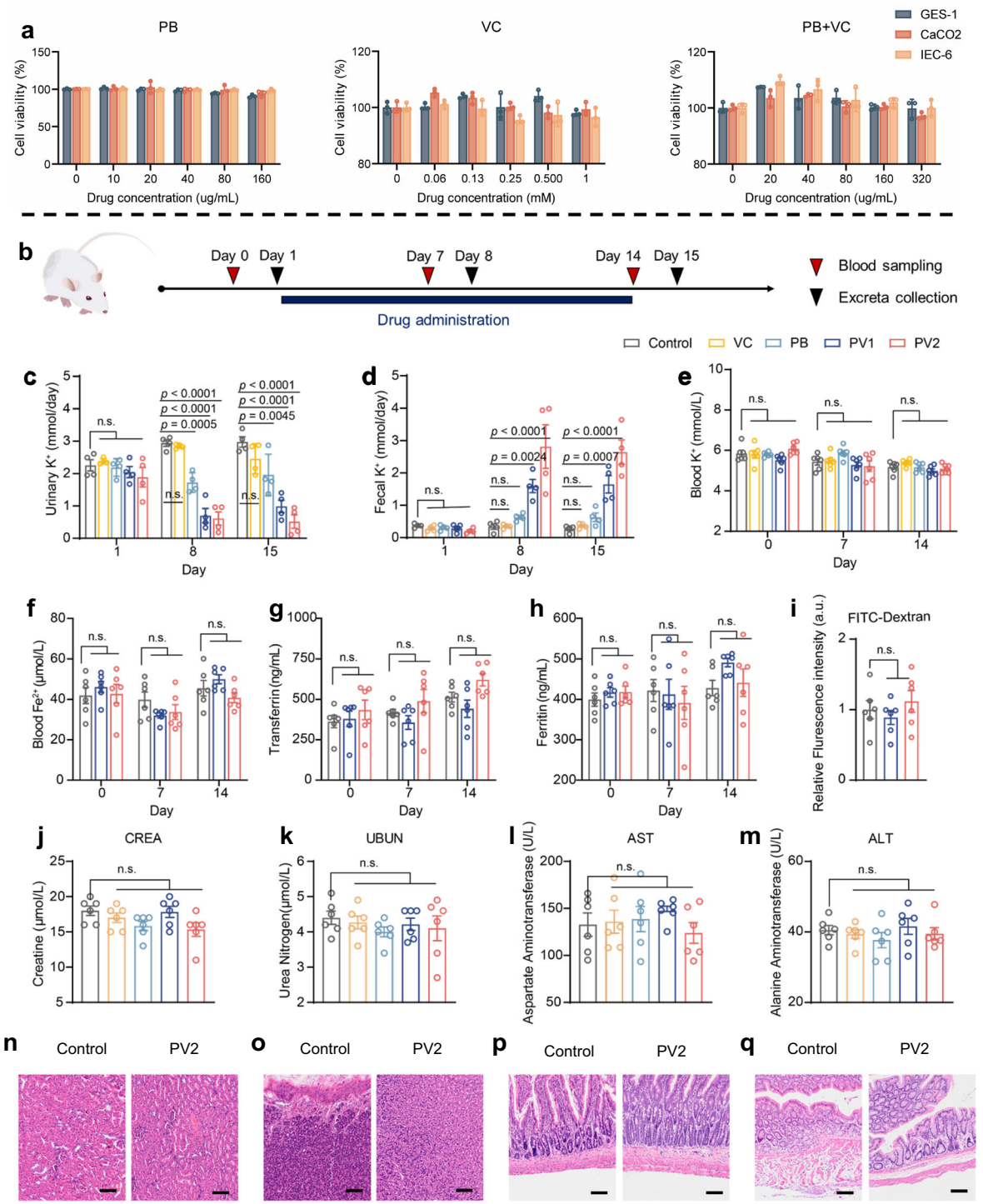

Fig. 4 | Assessment of biosafety of PB + VC. a In vitro cell viabilities of GES-1, IEC-6 and Caco-2 cells (gastrointestinal cells) after incubation of PB, VC, and PB + VC for 24 h (biological replicates, $n = 3$). **b** Experimental design for the safety study in male Sprague-Dawley (SD) rats. Rats were respectively administered with 6 g kg^{-1} PB, 6 g kg^{-1} VC, 4 g kg^{-1} PB + VC (PV1: 2 g kg^{-1} PB + 2 g kg^{-1} VC) or 12 g kg^{-1} PB + VC (PV2: 6 g kg^{-1} PB + 6 g kg^{-1} VC) over a 14-day administration period. Urinary K^+ (**c**) and Fecal K^+ (**d**) sampled on days 1, 8, and 15 (biological replicates, $n = 4$). Blood K^+ (**e**) and Blood Fe^{2+} (**f**), transferrin (**g**), ferritin **h** concentration sampled on days 0, 7, and 14 (biological replicates, $n = 6$). **i** On the final day, GI permeability was tested using FITC-dextran. Rats were orally administered FITC-dextran, and serum was collected to determine the fluorescence intensity of FITC (biological replicates, $n = 6$). Kidney function assessment on the 14th day, including creatine (CREA) **j** and urea nitrogen (UBUN) (**k**) (biological replicates, $n = 6$). Liver function assessment on 14th day, including aspartate aminotransferase (AST) (**l**) and alanine aminotransferase (ALT) **m** (biological replicates, $n = 6$). H&E-stained pathological sections of kidney, stomach, small intestine and colon for rats of control and PV2 in (**n**–**q**)) on the 14th day. All the H&E-stained pathological sections were repeated three times with similar results. Scale bar in (**j**–**m**): 100 μm. All data are presented as the mean ± S.E.M. Statistics in (**c**–**h**): Two-way ANOVA with multiple comparisons corrected using the Tukey test, with significance set at $p < 0.05$. Statistics in (**l**–**m**): One-way ANOVA with multiple comparisons corrected through the Dunnett test, with significance set at $p < 0.05$. Calculated p values are shown in the figures. Source data are provided as a Source Data file.

https://doi.org/10.1038/s41467-025-67803-4

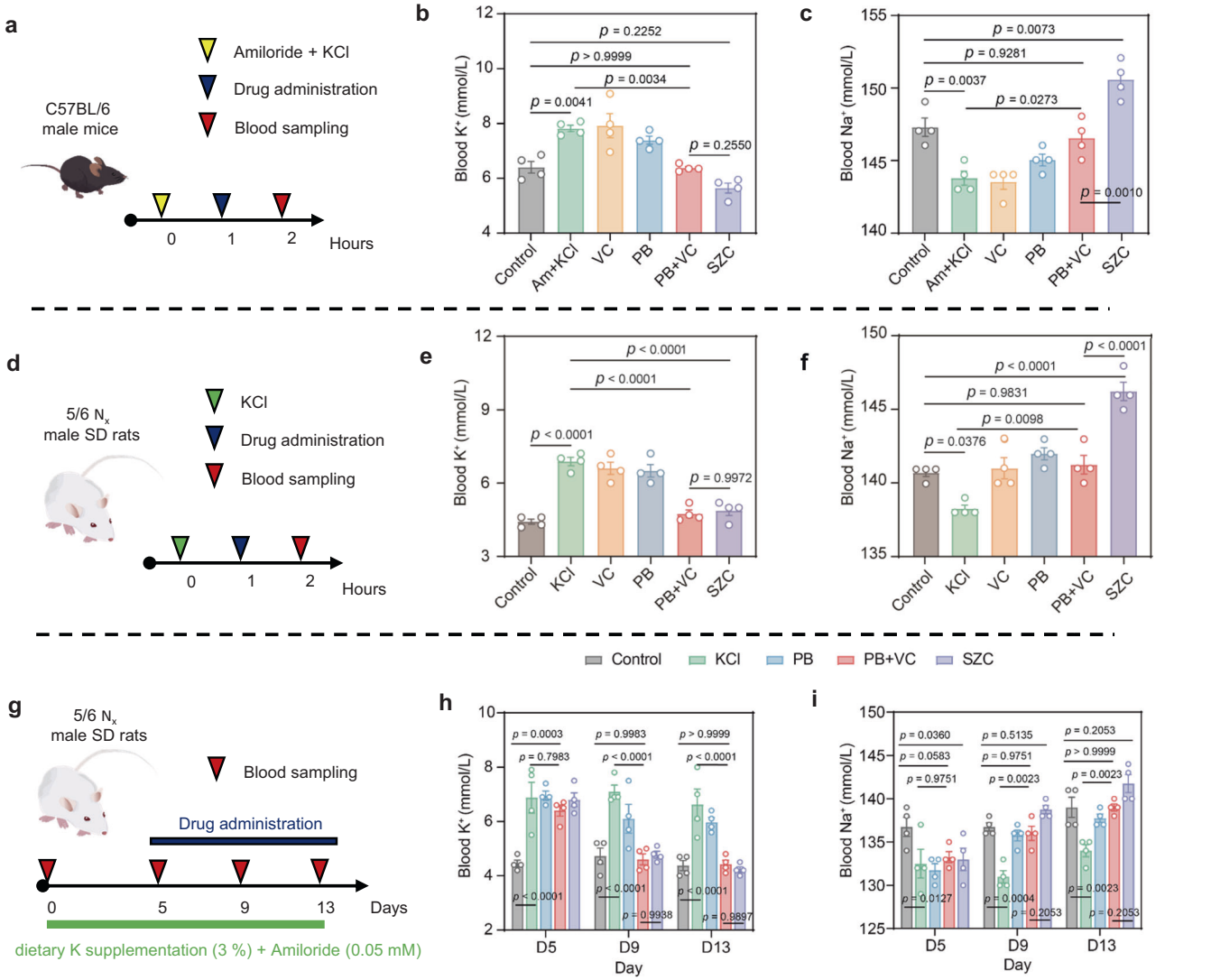

Fig. 5 | Evaluation of the therapeutic efficacy of PB + VC in the models of hyperkalemia. a Experimental design of the study of assessment in male C57BL/6 J mice. An intraperitoneal injection containing 0.03 wt% amiloride and 0.8 wt% KCl in dose of 10 μl g^{-1} was introduced to induce hyperkalemia. After 1 h, the administrations of PB + VC, PB, VC and SZC in dose of 4 g kg^{-1} per day. Blood K^+ (**b**) and Blood Na^+ **c** concentration sampled 1 h after intragastric gavage (biological replicates, $n = 4$). Experimental design of the study of assessment in male SD rats after 5/6 nephrectomy (N_x) for two animal models. **d** Gavage of fluid companied with KCl at a dose of 1 g kg^{-1} per day was introduced to induce acute hyperkalemia. After 1 h, drug administration of PB + VC, PB, VC, and SZC in dose of 4 g kg^{-1} per day. Blood K^+ (**e**) and Blood Na^+ (**f**) concentration sampled 1 h after intragastric gavage (biological replicates, $n = 4$). **g** Rats were switched to another purified, refined diet (AIN-93G) supplemented with additional K (3% weight/weight) only and in combination with amiloride (0.05 mM) for 14 days to induce chronic hyperkalemia. Drug administration of PB + VC, PB, and SZC in dose of 4 g kg^{-1} per day was started on day 5 for 8 days. Blood K^+ (**h**) and Blood Na^+ (**i**) concentration sampled 1 h after intragastric gavage (biological replicates, $n = 4$). All data are presented as the mean ± S.E.M. Statistics in (**b**, **c**, **e**, **f**): One-way ANOVA with multiple comparisons corrected through the Dunnett test, with significance set at $p < 0.05$. Statistics in (h-i): Two-way ANOVA with multiple comparisons corrected using the Tukey test, with significance set at $p < 0.05$. Calculated p values are shown in the figures. Source data are provided as a Source Data file.

staining of stomach, small intestine, and colon tissues harvested on day 14 confirmed that PB + VC did not affect the physiological function of healthy rats (Figs. 5n–q and S15). In conclusion, PB + VC was found to be safe in rats even at a high dose. This is well above the therapeutic dose of SZC administered to animals in current studies (approximately 4 g kg^{-1} in rats), indicating a wide therapeutic window for PB + VC[24,51–53].

The mechanism of action of amiloride involves blocking the epithelial sodium channel (ENaC) in the distal tubule of the kidney[54]. PHA-1 is commonly associated with hyperkalemia, which results from impaired ENaC function[55]. Given that both conditions involve a failure of ENaC function, we selected amiloride-induced hyperkalemia as a model to evaluate the efficacy of the drugs[56]. In contrast to the reduction in blood K^+ observed with SZC, which may be attributed to Na^+ release to alleviate amiloride-induced salt-wasting, as evidenced by the partial K^+-lowering effect of NaCl administration alone, PB + VC demonstrated efficacy in this model through direct adsorption, reducing blood K^+ to normal levels (Figs. 5a, b and S16)[57,58]. Additionally, amiloride caused only a mild, clinically insignificant decrease in blood Na^+ through K^+-sparing/Na^+-excreting. We hypothesize that PB + VC attenuates this change by restoring K^+ excretion and enhancing NHE3-mediated reabsorption of Na^+ in response to increased VC-derived H^+ concentration[59]. Concurrently, the Na^+ release by SZC led to elevated blood Na^+ levels, disrupting the electrolyte balance in mice (Fig. 5c).

Hyperkalemia is also commonly associated with impaired renal function and high-potassium diets. To mimic this disease and establish hyperkalemia models, we used male SD rats with chronic kidney disease (CKD) induced by 5/6 nephrectomy (N_x). Two distinct models

were developed: An acute hyperkalemia model induced by direct potassium chloride (KCl) administration and a chronic hyperkalemia model established through long-term high-potassium diet feeding (Fig. 5d, g)[52,60,61]. Both PB + VC and SZC were found effective in reversing the increase in blood K^+ levels (Fig. 5e, h). As anticipated, the PB + VC treatment, as a gut-restricted strategy based on metal counterion-free release, effectively corrected abnormal blood K^+ by promoting substantial fecal K^+ excretion. KCl supplementation moderately reduced blood Na^+ in rats, likely through tonic inactivation of NaCl cotransporter (a known antihypertensive mechanism) in the renal distal convoluted tubule[62]. This effect was exacerbated in the 5/6 N_x model due to impaired tubular Na^+ reabsorption from nephron loss. The K^+ excretion mechanism of PB + VC concurrently restored normal blood Na^+ (Fig. 5f, I).

Unlike SZC, which exacerbates renal metabolic stress through excessive Na^+ release, particularly detrimental given pre-existing nephron impairment where Na^+ metabolism competitively disrupts other electrolytes (e.g., Mg^{2+}), PB + VC not only corrects hyperkalemia-induced sodium imbalance but also prevents secondary electrolyte disturbances and metal counterion release, thereby avoiding additional renal metabolic burden (Figs. S17a, b, d, f and S18). Notably, PB + VC did not exacerbate acidosis, a frequent complication of hyperkalemia, and even demonstrated mild ameliorative effects during prolonged administration (Fig. S17c, f). This makes PB + VC a more suitable clinical treatment for hyperkalemia, particularly for patients with underlying health conditions such as CKD, PHA-1 and Gordon's syndrome (hyperkalemia-hypertension syndrome), due to its distinctive adsorption mechanism that avoids ion exchange. To sum up, PB + VC treatment for hyperkalemia in animal models is both safe and effective, with the potential for broader clinical applications.

Discussion

In this manuscript, PB was selected, and an in vivo reduction-induced ion-selective adsorption (IRISA) strategy was developed in combination with VC to directly adsorb K^+ without metal counterion release. Based on characterizations and theoretical studies, it can be inferred that the structural properties of PB, coupled with the presence of K^+, are key factors driving selective K^+ adsorption. Only in the presence of K^+ does VC induce changes in the valence state of Fe in PB, promoting K^+ adsorption. This process alters the spin state, oxidation state, electron density, and the chemical environment around the C≡N bond of the Fe nuclei in PB, significantly enhancing K^+ adsorption. PB + VC demonstrated excellent biocompatibility and therapeutic efficacy in both in vitro and in vivo studies. An unmet clinical need exists for metal ion-free potassium binders, as the release of metal counterions can exacerbate metabolic complications in hyperkalemia patient and the circulatory system dysfunction is common in such patients. By recapitulating electrochemical insertion dynamics in the GI tract, our strategy pioneers a therapeutic modality where reductants serve as voltage-driven in vivo, dynamically tuning material electronic states for ion adsorption. As the first demonstration of electrochemical therapy in the GI tract, this work addresses a long-standing limitation of traditional binders and establishes a paradigm for treating electrolyte disorders. Moreover, our strategy establishes a novel framework for managing metabolic disorders through in vivo electrochemical processes.

Methods

In vitro experiment part

Materials and chemicals. Prussian Blue ($Fe_7C_{18}N_{18}$, PB, >99.0%) and L(+)-Ascorbic Acid ($C_6H_8O_6$, Vitamin C, >99.0%) were purchased from Adamas-beta®. Sodium polystyrene sulfonate (SPS, Kayexalate®) was purchased from KALIMATE, calcium polystyrene sulfonate (CPS, Kalimate®) was purchased from SCOND. Sodium Zirconium Cyclosilicate Powder (Lokelma™) was purchased from AstraZeneca. Other reagents were purchased from Adamas-beta ® without any further purification.

Preparation of PB + VC. Briefly, PB (200 mg) and VC (200 mg) were mixed with MEI (40 mL), followed by incubation at 37 °C with orbital shaking (180 rpm) for 2 h. Post-incubation, the mixture was centrifuged at 1600 g for 5 min to separate the supernatant. The resulting pellet underwent three washing cycles with deionized water (30 mL per cycle, vortex mixing for 30 s), each followed by identical centrifugation parameters. The purified precipitate was flash-frozen in liquid nitrogen and subsequently lyophilized for 48 h to obtain the final product for Structural and morphological characterization. In the processed PB + VC, the VC component and its oxidation products dissolve in aqueous solution, yielding a final product consisting primarily of K^+-adsorbed PB.

Material characterizations. The textural properties of the samples were analyzed using the instruments listed below. The crystalline phase was characterized by X-ray diffraction (XRD, D8 Advance Da Vinci, Bruker, Germany) with 2θ ranging from 10° to 70°. The composition and structure of samples were recorded on Fourier transform infrared spectra (FT-IR, Nicolet 6700, ThermoFisher Scientific, USA) and Raman spectra (inVia Qontor, Renishaw, UK). Quantification of the elements in the samples was performed using wavelength disperse X-ray fluorescence (XRF, S8 Tiger II, BRUKER AXS GmbH, China). Specific surface area and porosity in N_2 were investigated with specific surface area and porosity analyzer (Autosorb-IQ3/EVO, Quantachrome, USA). Ultraviolet−visible (UV-vis) absorption spectra were collected using a CARY 5000 spectrophotometer (Lambda 950, PerkinElmer, USA). The 57Fe Mössbauer spectra of samples were recorded on Mössbauer spectrometer (SEE CoW304, Wissel, Germany) using a 57Co/Rh source in transmission geometry. The data were fitted by using the MossWinn 4.0 software. The chemical composition was analyzed by X-ray photoelectron spectroscopy (XPS, NEXSA, Thermofisher Scientific, USA).

Microscopy images: A small amount of powdered sample was first adhered to conductive tape and sputter-coated with gold for 45 s at 10 mA using a Quorum SC7620 sputter coater. Subsequently, the sample morphology was examined using a ZEISS GeminiSEM 300 (Germany) scanning electron microscope (SEM) at an accelerating voltage of 3 kV with an SE2 secondary electron detector, while EDS mapping was performed at 15 kV. For further analysis, another portion of the powder was embedded and ultrathin-sectioned for characterization using a FEI Talos F200X field-emission transmission electron microscope (TEM, USA) equipped with a BM Ceta camera. Both TEM imaging and EDS mapping were conducted at 200 kV, with the EDS system achieving an energy resolution of 136 eV. All TEM data were processed and analyzed using Velox software.

Ex-situ X-ray diffraction (XRD) data were collected using a D8 ADVANCE Da Vinci diffractometer with Cu Kα radiation (λ = 0.154 nm). Ex-situ Raman spectra were recorded in the 2500−500 cm^{-1} Raman shift region using Renishaw inVia Qontor. Both were treated with different concentrations of reducing agents.

Electrochemical measurements. Preparation of PB electrodes: 10 mg PB catalyst was added to 950 µL water, 950 µL ethanol and 50 µL Nafion solution, then sonicated for 15 min. The resulting 100 µL sample was dropped onto a clean ITO electrode, dried at room temperature.

The electrochemical adsorption performance of the electrode materials was studied by cyclic voltammetry (CV) (CHI 660E, CH Instruments Inc., USA). The platinum electrode was against electrode, reference electrode was Ag/AgCl electrode, electrolyte is different ionic solution and the voltage window is from −1. V to +1 V, and the scan rate is 50 mV s^{-1}.

Quantum chemical calculation. All the calculations are performed in the framework of the density functional theory with the projector augmented plane-wave method, as implemented in the Vienna ab initio simulation package (VASP)[63]. The crystal structures input (CIF files) were uploaded as attachments. The exchange-correlation potential was chosen as the generalized gradient approximation (GGA) proposed by Perdew, Burke, and Ernzerhof (PBE)[64]. The long range van der Waals interaction is described by the DFT-D3 approach[65]. The cut-off energy for plane wave is set to 500 eV. Furthermore, the Brillouin zone was sampled using a Monkhorst–Pack k-point mesh (56) with 5 × 5 × 5 k-points for lattice optimizations and 9 × 9 × 9 k-points for static density of states (DOS) calculations, respectively. The energy criterion is set to 10 − 6 eV in iterative solution of the Kohn-Sham equatio. All the structures are relaxed until the residual forces on the atoms have declined to less than 0.03 eV/Å.

In these calculations, model anhydrous structures with a face-centered cubic $F\bar{4}3m$ unit cell were assumed. Four compensating charges are mimicked in the reduced state. The absorption energy was calculated on the basis of the PB crystal inserting different atoms as absorbate, given as $E_{ad} = (E_{host/adsorbate} - E_{host} - n\ E_{adsorbate})/n$, and $E_{host/adsorbate}$, E_{host} and $E_{adsorbate}$ are the DFT total energies of the adsorbate on the host crystal, the host crystal and the adsorbate itself, respectively.

In vitro ions adsorption assays. The adsorption capacity of PB + VC was evaluated by weighing Prussian blue at a concentration of 5 mg/mL and adding it to a centrifuge tube containing the configured liquid, with different mass ratios ascorbic acid added as a reducing agent. Furthermore, the adsorption capacity of alternative adsorbents (PB, SZC, SPS, and CPS) was employed at a concentration of 5 mg/mL for comparative purposes. The treated tubes were subjected to shaking at 37 °C for a period of two h at 180 rpm. Following this, the liquid phase underwent filtration and dilution before being characterized by inductively coupled plasma emission spectroscopy (ICP-OES). For this study, a Thermo iCAP7600 inductively coupled plasma emission spectrometer was utilized.

Adsorption capacity calculation formula as specified below:

$$\text{Adsorption capacity} = (C_0 - C_e)\,V/m\ (\text{mmol/g})$$

C_0 = Initial concentration before adsorption (mmol/L)
C_e = Equilibrium concentration after adsorption (mmol/L)
V = Solution volume (L)
m = Mass of adsorbent (PB + VC, PB, SZC, SPS, and CPS) (g)
The components of the simulated fluids are listed below:

Multi-element isoelectric solution with K^+, Na^+, Ca^{2+}, Mg^{2+} (MEI). 50 mM KCl, 50 mM NaCl, 25 mM $CaCl_2$, and 25 mM $MgCl_2$ were dissolved and made up to 1 L with purified water.

Simulated gastric fluid electrolyte solution (SGF). 8.625 mM KCl, 1.125 mM KH_2PO_4, 31.25 mM $NaHCO_3$, 0.15 mM $MgCl_2$, 0.625 mM $(NH_4)_2CO_3$, 59 mM NaCl was mixed in 1000 mL of purified water. The pH was adjusted to 3 with 1 M HCl.[66]

Simulated intestinal fluid electrolyte solution (SIF). 8.5 mM KCl, 1 mM KH_2PO_4, 106.25 mM $NaHCO_3$, 0.4125 mM $MgCl_2$, and 48 mM NaCl was mixed in 1000 mL of purified water. The pH was adjusted to 7 with 1 M HCl[66].

Fasted-state simulated gastric fluids electrolyte solution (FaSSGF). 80 mM Sodium taurocholate, 20 mM Lecithin, 8.625 mM KCl, 1.125 mM KH_2PO_4, 31.25 mM $NaHCO_3$, 0.15 mM $MgCl_2$, 0.625 mM $(NH_4)_2CO_3$ and 34.2 mM NaCl was mixed in 1000 mL of purified water. The pH was adjusted to 1.6 with 1 M HCl or 1 M NaOH[67].

Fed-state simulated gastric fluids electrolyte solution (FeSSGF). 17.12 mM Acetic acid, 29.75 mM Sodium acetate, 8.625 mM KCl, 1.125 mM KH_2PO_4, 31.25 mM $NaHCO_3$, 0.15 mM $MgCl_2$, 0.625 mM $(NH_4)_2CO_3$ and 237.02 mM NaCl was mixed in 1000 mL of purified water. The pH was adjusted to 5.0 with 1 M HCl or 1 M NaOH[67].

Fasted-state simulated intestinal fluids electrolyte solution (FaSSIF). 3 mM Sodium taurocholate, 0.75 mM Lecithin, 8.5 mM KCl, 1 mM KH_2PO_4, 106.25 mM $NaHCO_3$, 8.7 mM NaOH, 28.7 mM NaH_2PO_4, 0.4125 mM $MgCl_2$ and 105.9 mM NaCl was mixed in 1000 mL of purified water. The pH was adjusted to 6.50 with 1 M HCl or 1 M NaOH[68].

Fed-state simulated intestinal fluids electrolyte solution (FeSSIF). 15 mM Sodium taurocholate, 3.75 mM Lecithin, 144 mM Glacial Acetic Acid, 8.5 mM KCl, 1 mM KH_2PO_4, 106.25 mM $NaHCO_3$, 101 mM NaOH, 0.4125 mM $MgCl_2$ and 173 mM NaCl was mixed in 1000 mL of purified water. The pH was adjusted to 5.0 with 1 M HCl or 1 M NaOH[68].

Simulated Colonic Fluids electrolyte solution (SCoF). 5.5900 g K_2HPO_4, 0.4100 g KH_2PO_4 was mixed in 1000 mL of purified water. The pH was adjusted to 7.8 with 1 M HCl or 1 M NaOH[67].

Fasted-state simulated colonic fluids (FaSSCoF). 0.0646 g sodium tauroglycocholate, 0.1932 g lecithin, 0.0305 g sodium oleate, 10.88 g NaOH, 5.4513 g tris(hydroxymethyl)aminomethane hydrochloride, 8.8210 g maleic acid, 5.5900 g K_2HPO_4, 0.4100 g KH_2PO_4 was mixed in 1000 mL of purified water. The pH was adjusted to 7.8 with 1 M HCl or 1 M NaOH.

Fed-state simulated colonic fluids (FeSSCoF). 0.2583 g sodium tauroglycocholate, 0.3219 g lecithin, 0.1609 g sodium oleate, 3.7600 g NaOH, 3.7553 g tris(hydroxymethyl)aminomethane hydrochloride, 3.4821 g maleic acid, 5.5900 g K_2HPO_4, 0.4100 g KH_2PO_4 was mixed in 1000 mL of purified water. The pH was adjusted to 6.0 with 1 M HCl or 1 M NaOH.

In vivo experiment part

Materials and chemicals. Rat Lipopolysaccharide (LPS) and Diamine Oxidase (DAO) ELISA kits were purchased from BYabscience (Nanjing, China). Rat Ferritin and transferrin ELISA kits were obtained from Jianglai Biotech (Shanghai, China). Purified, refined diet (AIN-93G) and refined diet (AIN-93G) supplemented with additional K (3% weight/weight) were purchased from Yihe Suyuan Bio-engineering (Nanjing, China).

Cell culture. Human gastric mucosal epithelial cells (GES-1), intestinal crypt epithelial cells (IEC-6) and human colon carcinoma cell line, Caco-2, was obtained from the National Collection of Authenticated Cell Cultures and cultivated in Dulbecco's modified Eagle's medium (DMEM) (Adamas life®) supplemented with 20% fetal bovine serum (FBS) (Adamas life®) and 1% antibiotic antimycotic solution (containing 10,000 units/ml penicillin G, 10 mg/ml streptomycin sulfate and 25 μg/ml amphotericin) (Adamas life®). All the cells were incubated at 37 °C in 5% CO2 atmosphere. Before each experiment, the cultures were washed with phosphate-buffered saline (PBS, pH 7.4) (Thermo Fisher Scientific), detached with 0.25% trypsin–ethylenediaminetetraacetic acid (EDTA) solution (Beyotime Biotechnology), and then centrifuged at 1000 rpm for 5 min, followed by resuspension.

Cytotoxicity evaluation. The cytotoxicity of samples against GES-1, IEC-6 and Caco-2 cells (GI cells) was evaluated by live/dead staining and CCK-8 assay. First, 1×10^5 GI cells were seeded in six-well plates, after incubation at 37 °C in a humidified atmosphere with 5% CO_2 for 24 h, the culture medium was replaced by PB, VC and PB + VC (each concentration, 160, 160, and 320 μg ml^-) for 24 h. Then, the cells were observed by a fluorescence microscope after being stained with

calcein-AM (acetoxymethyl) and propidium iodide (PI) (Adamas life®). Meanwhile, an CCK-8 assay was conducted to assess the cytotoxicity. A total of 5×10^3 GI cells were seeded in 96-well plates and cultured for 24 h. Then, cells were treated with a series of concentrations of PB, VC and PB + VC and incubated for 24 h. After CCK-8 (Yeasen) addition for 4 h, the OD values of each well were measured at 450 nm on an enzyme standard. The cell viability calculation is as follows: $(OD_{samples} - OD_{blank})/(OD_{control} - OD_{blank}) \times 100\%$.

Animals. All procedures were conducted in agreement with the guideline of the Institutional Animal Care and Use Committee (IACUC) of Shanghai Jiao Tong University. IACUC of Shanghai Jiao Tong University approved all protocols (No. 3 A2023215). Male SD rats (200 ~ 250 g body weight) were purchased from the Vital River Laboratory Animal Technology Co., Ltd (Nanjing, China). Male C57BL/6 mice (15–20 g body weight) were purchased from Jihui Laboratory Animal Care Co., Ltd (Shanghai, China). All animals were housed in an SPF facility at Shanghai Jiao Tong University and received human care. Prior to the experiments, the animals were maintained on a 12-hour light/dark cycle with constant temperature and humidity, and acclimated to the housing environment for at least seven days. Animals were randomly assigned to treatment groups using a random number generator. To control for potential covariates, such as body weight, animals were stratified before randomization to ensure equal distribution across groups.

Toxicity study in normal animals. All animal experiments and procedures were approved by the Institutional Animal Care and Use Committee of Shanghai Jiao Tong University. All SD rats were purchased from Shanghai Jihui Laboratory Animal Care Co., Ltd. 30 male rats were divided into 4 groups in the experiment. The control group received water intragastric injection twice a day during drug administration. As for 3 experimental groups, they respectively received 6 g kg^{-1} PB, 6 g kg^{-1} VC, 4 g kg^{-1} PB + VC (PV1: 2 g kg^{-1} PB + 2 g kg^{-1} VC) or 12 g kg^{-1} PB + VC (PV2: 6 g kg^{-1} PB + 6 g kg^{-1} VC) by intragastric injection twice a day, respectively.

1 h before the first intragastric administration on days 0, 7, and 14, whole blood samples (150 µL) were collected and analyzed using an automatic blood analyzer (XN-1000V, Sysmec Co., Japan). Approximately 100 µL whole blood samples were used for electrolyte concentration and arterial blood gas analysis. Indicators of respiratory function, acid-base balance, and plasma ions (K^+, Na^+, Ca^{2+}) were obtained in rats using a portable blood gas analyzer (iSTAT-300, Abbott Laboratories, USA) equipped with EG7+ chips (EG7 + , Abbott Laboratories, USA).

About 1 mL blood samples were put into a centrifuge tube, standing for 1 h, and then the samples were centrifuged for 10 min at a speed of 1600 g to collect serum. The serum (~200 µL) was used in the test of Mg^{2+}, Fe^{2+}, kidney function and liver function by automated analyzer including software (Cobas c 311, Roche Diagnostics, USA). ELISA Ferritin, transferrin, DAO, and LPS kits were used according to manufacturer's instructions.

Stool and urine samples were collected on days 1, 8, and 15 of the experiment. All stool and urine samples were digested in nitric acid and hydrogen peroxide prior to analysis. K^+, Na^+, Ca^{2+}, Mg^{2+} concentration of stool and urine were analyzed on the ICP-MS (NexION2, PerkinElmer, USA) spectrometer after digestion.

At the end of the experiment, rats were treated with FITC-dextran (300 mg kg^{-1}, p.o.) and whole blood was collected through orbits after 3 h for further testing. Then the rats were euthanized by CO_2. GI tracts were isolated and pathological sections were prepared to evaluate possible toxicity of the drugs.

Urinalysis of rats: Selected rats were placed in cages for 24 h to collect urine samples. Midstream urine samples were collected from rats during urination, mixed 5 thoroughly, and 2 mL of the sample was used for urinalysis using an automated urine biochemical analyzer (URIT-500B, URIT, China). The rest data were semi-quantitative results. Semi-quantitative results in urine analysis were converted into scores as follows: urinary protein (0: not detected, 1: <0.15 g/L, 2: <0.3 g/L, 3: <1.0 g/L), urinary glucose (0: not detected, 1: <2.8 mmol/L, 2: <5.5 mmol/L, 3: 14 mmol/L).

Efficacy study in mice and rats with high blood K^+. First, hyperkalemia was induced in 20 normal female C57BL/6 mice by intraperitoneal injection of 0.8 wt% KCl and 0.03 wt% amiloride (Adamas life®) and these mice were divided into 5 groups in the experiment[56]. The dose of intraperitoneal injection was 10 µl/g. 4 groups were followed by respectively intragastric injection of 4 g kg^{-1} PB, 4 g kg^{-1} VC, 4 g kg^{-1} PB + VC (2 g kg^{-1} PB + 2 g kg^{-1} VC) or 4 g kg^{-1} SZC per day. 4 normal control mice received intragastric injection of deionized water.

Second, at the beginning of the experiment, Sprague-Dawley (SD) rats with chronic kidney disease were induced in male SD rats by 5/6 subtotal nephrectomy (N_x) 21 days before the experiment[61]. KCl solution was used by intragastric injection to evaluate the therapeutic effect of this drug on acute hyperkalemia under the condition of a high-potassium diet in chronic kidney disease. Then, 25 nephrectomized rats were divided into 1 control group, 1 blank group, and 4 experimental groups. Rats in 4 experimental groups respectively received 4 g kg^{-1} PB, 4 g kg^{-1} VC, 4 g kg^{-1} PB + VC (2 g kg^{-1} PB + 2 g kg^{-1} VC) or 4 g kg^{-1} SZC per day. The control group received intragastric injection of water, and the blank group received KCl solution.

Third, refined diet (AIN-93G) supplemented with additional K (3% weight/weight) only and in combination with amiloride (0.05 mM) was used to evaluate the therapeutic effect of this drug on chronic hyperkalemia under the condition of a high-potassium diet in chronic kidney disease[60]. 16 nephrectomized rats were divided into 1 control group, 1 blank group, and 3 experimental groups. The control group received refined diet, and other group received high-potassium diet high-potassium diet for 14 days. Rats in experimental groups respectively received 4 g kg^{-1} PB, 4 g kg^{-1} PB + VC (2 g kg^{-1} PB + 2 g kg^{-1} VC) or 4 g kg^{-1} SZC per day was started on day 5 for 8 days.

All the Blood samples were collected 1 h after the intragastric injection of drugs. K^+, Na^+, Ca^{2+} were analyzed on the Abbot iSTAT1 analyzer with EG7+ chips. Mg^{2+} was analyzed on automated analyzer including software.

The effects of NH_4^+ and Na^+ in the amiloride-induced hyperkalemia model. Hyperkalemia was induced in 9 normal male C57BL/6 mice by intraperitoneal injection of 0.8 wt% KCl and 0.03 wt% amiloride (Am) and these mice were divided into 3 groups in the experiment. The dose of intraperitoneal injection was 10 µl/g. As for 3 experimental groups, they respectively received deionized water, 1.79 g kg^{-1} NaCl and 1 g kg^{-1} NH_4Cl per day by intragastric injection, divided into two daily doses administered after1 h and 5 h apart.

All the Blood samples were collected 1 h after the intragastric injection of drugs. K^+, Na^+ were analyzed on the Abbot iSTAT1 analyzer with EG7+ chips.

Statistical analysis

All experiments were performed at least triplicated with repeated measures. The results are expressed either as means ± standard error of the mean (S.E.M). One-way ANOVA with Tukey's multiple comparison test were used for testing differences among groups. For each statistical analysis, the sample size was greater or equal to three ($n \geq 3$). Detailed statistics can also be found in figure legends. Data were approximately normally distributed, and the variance was similar among all the groups. No samples were excluded from the analysis, and no preprocessing of data was performed before statistical analysis. Statistical significance is indicated as n.s. $p >= 0.5$ and precise p values were calculated and showed in figures.

Reporting summary

Further information on research design is available in the Nature Portfolio Reporting Summary linked to this article.

Data availability

The authors declare that the data supporting the findings of this study are available within the paper and its supplementary information files. The raw Raman data is included in the Source Data Excel file. Source data are provided with this paper.

References

1. Einhorn, L. M. et al. The frequency of hyperkalemia and its significance in chronic kidney disease. *Arch. Intern. Med.* **169**, 1156–1162 (2009).
2. Salem, M. M., Rosa, R. M. & Batlle, D. C. Extrarenal potassium tolerance in chronic renal failure: implications for the treatment of acute hyperkalemia. *Am. J. Kidney Dis.* **18**, 421–440 (1991).
3. Kovesdy, C. P. Epidemiology of hyperkalemia: an update. *Kidney Int. Suppl.* **6**, 3–6 (2016).
4. Cai, J. J., Wang, K., Jiang, H. Q. & Han, T. Characteristics, risk factors, and adverse outcomes of hyperkalemia in acute-on-chronic liver failure patients. *Biomed. Res. Int.* **2019**, 6025726 (2019).
5. Ratanasrimetha, P., Workeneh, B. T. & Seethapathy, H. Sodium and potassium dysregulation in the patient with cancer. *Adv. Chronic Kidney Dis.* **29**, 171–179.e171 (2022).
6. Goia-Nishide, K., Coregliano-Ring, L. & Rangel, ÉB. Hyperkalemia in diabetes mellitus setting. *Diseases* **10**, 20 (2022).
7. Udensi, U. K. & Tchounwou, P. B. Potassium homeostasis, oxidative stress, and human disease. *Int J. Clin. Exp. Physiol.* **4**, 111–122 (2017).
8. Palmer, B. F. & Clegg, D. J. Physiology and pathophysiology of potassium homeostasis: core curriculum 2019. *Am. J. Kidney Dis.* **74**, 682–695 (2019).
9. Valdivielso, J. M. et al. Hyperkalemia in Chronic Kidney Disease in the New Era of Kidney Protection Therapies. *Drugs* **81**, 1467–1489 (2021).
10. Weir, M. R. et al. Patiromer in patients with kidney disease and hyperkalemia receiving RAAS inhibitors. *N. Engl. J. Med.* **372**, 211–221 (2015).
11. Hoy, S. M. Sodium zirconium cyclosilicate: a review in hyperkalaemia. *Drugs* **78**, 1605–1613 (2018).
12. Montaperto, A. G., Gandhi, M. A., Gashlin, L. Z. & Symoniak, M. R. Patiromer: a clinical review. *Curr. Med. Res. Opin.* **32**, 155–164 (2016).
13. Labriola, L. & Jadoul, M. Sodium polystyrene sulfonate: still news after 60 years on the market. *Nephrol. Dial. Transplant.* **35**, 1455–1458 (2020).
14. Natale, P., Palmer, S. C., Ruospo, M., Saglimbene, V. M. & Strippoli, G. F. Potassium binders for chronic hyperkalaemia in people with chronic kidney disease. *Cochrane Database Syst. Rev.* **6**, Cd013165 (2020).
15. Joo, M., Bae, W. K., Kim, N. H. & Han, S. R. Colonic mucosal necrosis following administration of calcium polystryrene sulfonate (Kalimate) in a uremic patient. *J. Korean Med. Sci.* **24**, 1207–1211 (2009).
16. Sterns, R. H., Rojas, M., Bernstein, P. & Chennupati, S. Ion-exchange resins for the treatment of hyperkalemia: Are they safe and effective? *J. Am. Soc. Nephrol.* **21**, 733–735 (2010).
17. Nakamura, T. et al. Risks and Benefits of Sodium Polystyrene Sulfonate for Hyperkalemia in Patients on Maintenance Hemodialysis. *Drugs R. D.* **18**, 231–235 (2018).
18. Yu, M.-Y., Yeo, J. H., Park, J.-S., Lee, C. H. & Kim, G.-H. Long-term efficacy of oral calcium polystyrene sulfonate for hyperkalemia in CKD patients. *PLoS One* **12**, e0173542 (2017).
19. Meaney, C. J., Beccari, M. V., Yang, Y. & Zhao, J. Systematic review and meta-analysis of patiromer and sodium zirconium cyclosilicate: a new armamentarium for the treatment of hyperkalemia. *Pharmacotherapy* **37**, 401–411 (2017).
20. Rosano, G. M. C., Spoletini, I. & Agewall, S. Pharmacology of new treatments for hyperkalaemia: patiromer and sodium zirconium cyclosilicate. *Eur. Heart J. Suppl.* **21**, A28–A33 (2019).
21. Montagnani, A., Frasson, S., Gussoni, G. & Manfellotto, D. Optimization of RAASi therapy with new potassium binders for patients with heart failure and hyperkalemia: rapid review and meta-analysis. *J. Clin. Med.* **10**, 5483 (2021).
22. Desai, N. R. et al. The association of heart failure and edema events between patients initiating SZC or Patiromer. *Kidney360* (2024).
23. Khandelwal, P. et al. Safety and efficacy of sodium zirconium cyclosilicate for the management of acute and chronic hyperkalemia in children with chronic kidney disease 4-5 and on dialysis. *Pediatr. Nephrol.* **39**, 1213–1219 (2024).
24. Li, L., Budden, J., Quinn, C. M. & Bushinsky, D. Effects of patiromer and sodium zirconium cyclosilicate on blood pressure in rats with chronic kidney disease. *J. Cardiovasc. Pharmacol. Therapeutics* **29**, 10742484241227580 (2024).
25. Weiner, I. D. Roles of renal ammonia metabolism other than in acid-base homeostasis. *Pediatr. Nephrol.* **32**, 933–942 (2017).
26. Xiang, L. et al. Synergistic machine learning accelerated discovery of nanoporous inorganic crystals as non-absorbable oral drugs. *Adv. Mater.* **36**, 2404688 (2024).
27. Kumar, R. et al. Persistent hyperammonemia is associated with complications and poor outcomes in patients with acute liver failure. *Clin. Gastroenterol. Hepatol.* **10**, 925–931 (2012).
28. Xie, Y., Lin, R. B. & Chen, B. Old materials for new functions: recent progress on metal cyanide based porous materials. *Adv. Sci.* **9**, e2104234 (2022).
29. Xu, C. et al. Prussian blue analogues in aqueous batteries and desalination batteries. *Nanomicro Lett.* **13**, 166 (2021).
30. Estelrich, J. & Busquets, M. A. Prussian blue: a safe pigment with zeolitic-like activity. *Int J Mol Sci* **22** (2021).
31. Matsuda, T., Takachi, M. & Moritomo, Y. A sodium manganese ferrocyanide thin film for Na-ion batteries. *Chem. Commun.* **49**, 2750–2752 (2013).
32. Shu, W., Han, C. & Wang, X. Prussian blue analogues cathodes for nonaqueous potassium-ion batteries: past, present, and future. *Adv. Funct. Mater.* **34**, 2309636 (2024).
33. Kulesza, P. J., Zamponi, S., Berrettoni, M., Marassi, R. & Malik, M. A. Preparation, spectroscopic characterization and electrochemical charging of the sodium-containing analogue of Prussian Blue. *Electrochim. Acta* **40**, 681–688 (1995).
34. Karyakin, A. A., Karyakina, E. E. & Gorton, L. On the mechanism of H2O2 reduction at Prussian Blue modified electrodes. *Electrochem. Commun.* **1**, 78–82 (1999).
35. Thompson, D. F. & Callen, E. D. Soluble or insoluble prussian blue for radiocesium and thallium poisoning? *Ann. Pharmacother.* **38**, 1509–1514 (2004).
36. Hoffman, R. S. Thallium toxicity and the role of Prussian blue in therapy. *Toxicol. Rev.* **22**, 29–40 (2003).
37. Mohammad, A., Yang, Y., Khan, M. A. & Faustino, P. J. Long-term stability study of Prussian blue—A quality assessment of water content and cyanide release. *Clin. Toxicol.* **53**, 102–107 (2015).
38. Peng, J. et al. Prussian blue analogues for sodium-ion batteries: past, present, and future. *Adv. Mater.* **34**, e2108384 (2022).
39. Ma, F., Li, Q., Wang, T., Zhang, H. & Wu, G. Energy storage materials derived from Prussian blue analogues. *Sci. Bull. (Beijing)* **62**, 358–368 (2017).
40. Liu, Y. et al. Isostructural synthesis of iron-based Prussian blue analogs for sodium-ion batteries. *Small* **19**, e2302687 (2023).
41. Guo, T. et al. Competitive adsorption of alkali metal ions onto Prussian blue. *Desalin. Water Treat.* **272**, 118–125 (2022).
42. Padayatty, S. J. et al. Vitamin C pharmacokinetics: implications for oral and intravenous use. *Ann. Intern. Med.* **140**, 533–537 (2004).

43. Camarena, V. & Wang, G. The epigenetic role of vitamin C in health and disease. *Cell Mol. Life Sci.* **73**, 1645–1658 (2016).
44. Pearce, J. Studies of any toxicological effects of Prussian blue compounds in mammals–a review. *Food Chem. Toxicol.* **32**, 577–582 (1994).
45. Gerber, S. J. & Erasmus, E. Electronic effects of metal hexacyanoferrates: an XPS and FTIR study. *Mater. Chem. Phys.* **203**, 73–81 (2018).
46. Kettle, S. F. A., Diana, E., Marchese, E. M. C., Boccaleri, E. & Stanghellini, P. L. The vibrational spectra of the cyanide ligand revisited: the ν(CN) infrared and Raman spectroscopy of Prussian blue and its analogues. *J. Raman Spectrosc.* **42**, 2006–2014 (2011).
47. Benzie, I. F. F. & Strain, J. J. in *Methods in Enzymology* Vol. 299, 15-27 (Academic Press, 1999).
48. Hidalgo, I. J., Raub, T. J. & Borchardt, R. T. Characterization of the human colon carcinoma cell line (Caco-2) as a model system for intestinal epithelial permeability. *Gastroenterology* **96**, 736–749 (1989).
49. Lotfollahi, Z. et al. Comparative effects of mistletoe extracts in combination with 5-Fluorouracil on viability of IEC-6 and Caco-2 intestinal epithelial cells. *Aust. J. Herb. Naturopathic. Med.* **30**, 174–179 (2018).
50. Ding, Y. et al. Tissue distribution of polystyrene nanoplastics in mice and their entry, transport, and cytotoxicity to GES-1 cells. *Environ. Pollut.* **280**, 116974 (2021).
51. Rafique, Z., Peacock, W. F., LoVecchio, F. & Levy, P. D. Sodium zirconium cyclosilicate (ZS-9) for the treatment of hyperkalemia. *Expert Opin. Pharmacother.* **16**, 1727–1734 (2015).
52. Marmol, F. et al. Fecal ammonium in mice with CKD: gastrointestinal sequestration by sodium zirconium cyclosilicate. *Am. J. Physiol. Ren. Physiol.* **324**, F464–f471 (2023).
53. Ash, S. R., Singh, B., Lavin, P. T., Stavros, F. & Rasmussen, H. S. A phase 2 study on the treatment of hyperkalemia in patients with chronic kidney disease suggests that the selective potassium trap, ZS-9, is safe and efficient. *Kidney Int.* **88**, 404–411 (2015).
54. Teiwes, J. & Toto, R. D. Epithelial sodium channel inhibition in cardiovascular disease*: a potential role for amiloride. *Am. J. Hypertens.* **20**, 109–117 (2007).
55. Bonny, O., Knoers, N., Monnens, L. & Rossier, B. C. A novel mutation of the epithelial Na+ channel causes type 1 pseudohypoaldosteronism. *Pediatr. Nephrol.* **17**, 804–808 (2002).
56. Borok, Z., Schneider, S. M., Fraley, D. S. & Adler, S. A rat model for hyperkalemia. *Proc. Soc. Exp. Biol. Med* **185**, 39–40 (1987).
57. Pradervand, S. et al. Salt restriction induces pseudohypoaldosteronism type 1 in mice expressing low levels of the beta-subunit of the amiloride-sensitive epithelial sodium channel. *Proc. Natl. Acad. Sci. USA* **96**, 1732–1737 (1999).
58. Stone, R. C., Vale, P. & Rosa, F. C. Effect of hydrochlorothiazide in pseudohypoaldosteronism with hypercalciuria and severe hyperkalemia. *Pediatr. Nephrol.* **10**, 501–503 (1996).
59. Orlowski, J. & Grinstein, S. Na+/H+ exchangers. *Compr. Physiol.* **1**, 2083–2100 (2011).
60. Iyer, S. P. N., Lee, L. & Li, L. Pharmacodynamic effects of the K(+) binder patiromer in a novel chronic hyperkalemia model in spontaneously hypertensive rats. *Physiol. Rep.* **8**, e14572 (2020).
61. Li, L. et al. Mechanism of action and pharmacology of patiromer, a nonabsorbed cross-linked polymer that lowers serum potassium concentration in patients with hyperkalemia. *J. Cardiovasc Pharm. Ther.* **21**, 456–465 (2016).
62. Rengarajan, S. et al. Increasing plasma [K+] by intravenous potassium infusion reduces NCC phosphorylation and drives kaliuresis and natriuresis. *Am. J. Physiol. Ren. Physiol.* **306**, F1059–F1068 (2014).
63. Kresse, G. & Joubert, D. From ultrasoft pseudopotentials to the projector augmented-wave method. *Phys. Rev. B* **59**, 1758–1775 (1999).
64. Perdew, J. P., Burke, K. & Ernzerhof, M. Generalized gradient approximation made simple. *Phys. Rev. Lett.* **77**, 3865–3868 (1996).
65. Grimme, S., Antony, J., Ehrlich, S. & Krieg, H. A consistent and accurate ab initio parametrization of density functional dispersion correction (DFT-D) for the 94 elements H-Pu. *J. Chem. Phys.* **132**, 154104 (2010).
66. Jakobek, L. et al. Simulated Gastric and Intestinal Fluid Electrolyte Solutions as an Environment for the Adsorption of Apple Polyphenols onto β-Glucan. *Molecules* **27**, 6683 (2022).
67. Marques, M. R. C., Loebenberg, R. & Almukainzi, M. Simulated biological fluids with possible application in dissolution testing. *Dissolution Technol.* **18**, 15–28 (2011).
68. Dahlgren, D. et al. Fasted and fed state human duodenal fluids: Characterization, drug solubility, and comparison to simulated fluids and with human bioavailability. *Eur. J. Pharm. Biopharm.* **163**, 240–251 (2021).

Acknowledgements

This work was supported by Shanghai Municipal Science and Technology Major Project, the National Natural Science Foundation of China (grant no. 22171184 and T2550061) and Young Leading Scientists Cultivation Plan supported by Shanghai Municipal Education Commission (ZXWH1082101). The authors would like to thank Shenzhen HUASUAN Technology Co., Ltd. for assistance with DFT calculations. The authors would like to thank Yan Zhu from Shanghai Jiao Tong University Instrumental Analysis Center with elemental analysis testing. The authors would like to thank Xiaoxun Huang from Shiyanjia Lab (www.shiyanjia.com) for the BET analysis. The authors would like to thank Shanghai Jiao Tong University Laboratory Animal Center for Animal Feeding Services.

Author contributions

Y.W., L.X., and S.Z. designed the material and experiments. Y.W., Y.X., T.L., X.C., F.T. and L.X. prepared and characterized the materials. Y.W. and L.X. performed the in vitro experiment. Y.W., J.Z., Z.L., and L.X. performed the in vivo evaluation of the materials. Y.W., X.Z., and L.X. analyzed the data. Y.W., L.X., and S.Z. wrote the paper. S.Z. supervised the research. All authors discussed the progress of the research and reviewed the manuscript. Y.W. and L.X. contributed equally to this work.

Competing interests

The authors declare no competing interests.

Additional information

Supplementary information The online version contains supplementary material available at https://doi.org/10.1038/s41467-025-67803-4.

Correspondence and requests for materials should be addressed to Shiyi Zhang.

Peer review information *Nature Communications* thanks Ewout Hoorn, who co-reviewed with Sebastian Beckmann and the other anonymous reviewer(s) for their contribution to the peer review of this work. A peer review file is available.

Reprints and permissions information is available at http://www.nature.com/reprints

Publisher's note Springer Nature remains neutral with regard to jurisdictional claims in published maps and institutional affiliations.

Open Access This article is licensed under a Creative Commons Attribution-NonCommercial-NoDerivatives 4.0 International License, which permits any non-commercial use, sharing, distribution and reproduction in any medium or format, as long as you give appropriate credit to the original author(s) and the source, provide a link to the Creative Commons licence, and indicate if you modified the licensed material. You do not have permission under this licence to share adapted material derived from this article or parts of it. The images or other third party material in this article are included in the article's Creative Commons licence, unless indicated otherwise in a credit line to the material. If material is not included in the article's Creative Commons licence and your intended use is not permitted by statutory regulation or exceeds the permitted use, you will need to obtain permission directly from the copyright holder. To view a copy of this licence, visit http://creativecommons.org/licenses/by-nc-nd/4.0/.

© The Author(s) 2025